actuators

MDPI

Article

Thermal Behavior of a Magnetically Levitated Spindle for Fatigue Testing of Fiber Reinforced Plastic

Daniel Franz *, Maximilian Schneider, Michael Richter and Stephan Rinderknecht

Institute for Mechatronic Systems in Mechanical Engineering, Technische Universität Darmstadt, 64287 Darmstadt, Germany; schneider@ims.tu-darmstadt.de (M.S.); richter@ims.tu-darmstadt.de (M.R.); rinderknecht@ims.tu-darmstadt.de (S.R.)

* Correspondence: franz@ims.tu-darmstadt.de

† This paper is an extended version of our paper published in: Franz, D.; Schneider, M.; Richter, M.; Rinderknecht, S. Magnetically levitated spindle for long term testing of fiber reinforced plastic. In Proceedings of the 16th International Symposium on Magnetic Bearings (ISMB16), Beijing, China, 13–17 August 2018.

Received: 3 April 2019; Accepted: 30 April 2019; Published: 3 May 2019

Abstract: This article discusses the critical thermal behavior of a magnetically levitated spindle for fatigue testing of cylinders made of fiber reinforced plastic. These cylinders represent the outer-rotor of a kinetic energy storage. The system operates under vacuum conditions. Hence, even small power losses in the rotor can lead to a high rotor temperature. To find the most effective way to keep the rotor temperature under a critical limit in the existing system, first, transient electromagnetic finite element simulations are evaluated for the active magnetic bearings and the electric machine. Using these simulations, the power losses of the active components in the rotor can be derived. Second, a finite element simulation characterizes the thermal behavior of the rotor. Using the power losses calculated in the electromagnetic simulation, the thermal simulation provides the temperature of the rotor. These results are compared with measurements from an experimental spindle. One effective way to reduce rotational losses without major changes in the hardware is to reduce the bias current of the magnetic bearings. Since this also changes the characteristics of the magnetic bearings, the dynamic behavior of the rotor is also considered.

Keywords: active magnetic bearings; kinetic energy storage; fiber reinforced plastic; fatigue testing; thermal behavior

1. Introduction

Flywheels store energy as kinetic energy of the rotor and can provide a cost efficient solution for short-term energy storage and load smoothening services in electricity grids (e.g., [1,2]). Their advantages lie in the high possible number of cycles and the low initial cost per unit of power. The main drawbacks are their high stand-by-losses and the relatively low energy density compared to other storage technologies. In order to utilize the advantages, the energy density of one system should be increased while decreasing the stand-by losses at the same time.

1.1. Outer-Rotor Fywheel Design

One possible flywheel design is an outer-rotor setup (e.g., [3–5]). It promises high energy densities due to the large radii of the rotor and high rotational speeds. A realized full-scale system is described in [6]. A model of the system is shown in Figure 1a. The rotor is a magnetically levitated hollow cylinder. The outside of the rotor is made out of fiber reinforced plastic (FRP) with a circumferential fiber orientation, using carbon fibers. The inside of the rotor consists of different rotor parts of the

active and passive components. Active magnetic bearings (AMBs) are used for radial levitation and a passive magnetic bearing is used for axial levitation. A permanent magnet synchronous machine (PMSM) accelerates and decelerates the rotor. All rotating components of the magnetic bearings and the PMSM are integrated on the inner circumference of the FRP rotor. Under rotation, these components press against the FRP, resulting in radial compressive stress transversal to the fiber orientation, which is superimposed by circumferential stress in the fiber direction (see Figure 1b). The energy density of the system increases with the radii of the rotor and its rotational speed, both factors lead to an increased stress in the FRP [7]. Consequently, high stress in the material is necessary to reach high energy densities. Charging and discharging the flywheel leads to cyclically varying mechanical stresses. To investigate the cyclic stability and lifetime of the FRP rotor, cyclic material tests, such as cyclic transverse tensile tests (derived from [8]), cyclic transverse compressive tests (derived from [9]), and cyclic four-point bending tests are performed on material samples. These samples are thin walled and relatively easy to fabricate with a high quality, whereas the rotor of the flywheel is much thicker and harder to produce in an industrial fiber winding process. Furthermore, the thermal expansion of carbon fiber and the epoxy plastic matrix used differ, leading to inner stress when a thick walled FRP structure cools down from the curing temperature. Hence, there is a much higher probability of imperfections and defects in the thick walled FRP structure of an outer-rotor flywheel than in the thin material samples. Therefore, the applicability of test results obtained with thin material samples to the rotor of the flywheel has to be investigated by tests with thick walled rotors. A specialized test rig was designed and set up to perform cyclic tests on thick-walled FRP specimens, which represent the outer-rotor of kinetic energy storage. These specimens are smaller, cheaper and have a lower energy content, reducing the danger during destructive testing.

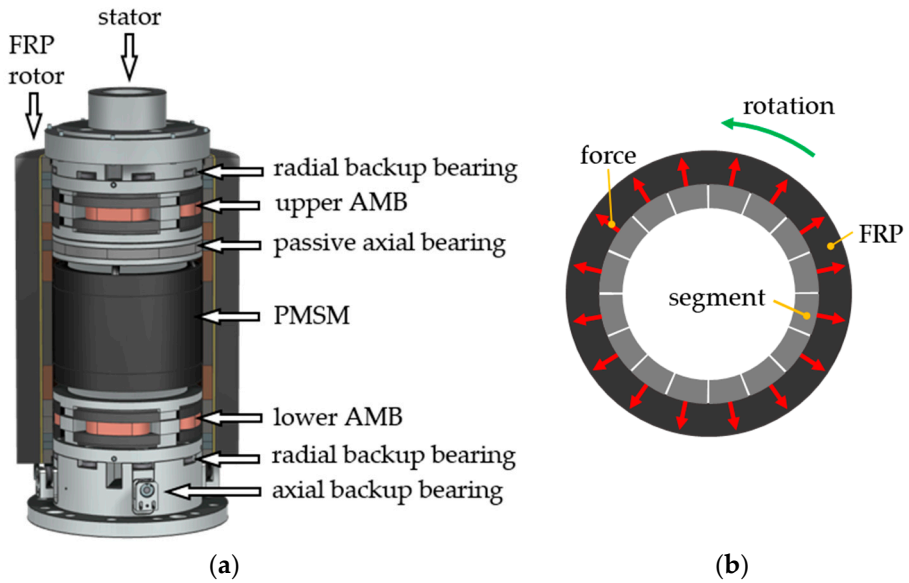

Figure 1. (**a**) Model the outer-rotor Flywheel described in [6] with a halved rotor; (**b**) Top view on the rotor showing the segments pressing against the fiber reinforced plastic (FRP) under rotation.

1.2. Testing Procedure

The ratio between the circumferential and the radial stress in a test specimen should be as close as possible to the one present in a full-scale flywheel. In the system described in [6], the radial transverse compressive stress in the FRP is 60 MPa and the circumferential longitudinal stress is 389 MPa at its maximum speed of 15,000 rpm. In the design of the flywheel, the maximum stress was limited to half of the expected strength of the FRP, to account for the high data uncertainty. To test the limits of the FRP, the stress in the specimen is doubled compared to the flywheel. To create this state of stress in the test specimen, a circumferentially segmented steel ring is placed inside the FRP cylinder of the

specimen, and rotated at 30,000 rpm. This results in a transverse compressive stress of 100 MPa and a longitudinal tension of 775 MPa in the FRP. With an outer diameter of 190 mm, the surface speed of the specimen reaches approximately 298 m/s. The fatigue test will be conducted by alternating between a maximum speed of 30,000 rpm and a minimum speed of 15,000 rpm. At minimum speed the transversal compressive stress is 26 MPa and the longitudinal tension is 200 MPa. Because of the well-known high tensile strength of carbon fiber, the chance of fiber fracture is low at this state of stress. The probability of matrix fracture is expected to be much higher [10]. It is planned to perform up to 200,000 cycles per specimen. With a cycle time of 30 s this will take about 70 days. Additionally, overload tests are planned, where the specimen is accelerated to 40,000 rpm, resulting in a surface speed of nearly 398 m/s, a circumferential longitudinal tension of 1,400 MPa and a radial compressive stress of 180 MPa. The latter should lead to failure of the matrix. In the longitudinal direction, the FRP can withstand static tensions over 2,000 MPa. To reduce air drag and the consequential heating of the specimen, all tests are performed under vacuum conditions, with a pressure below 0.05 Pa.

1.3. Test Rig Description

Figure 2a shows a section view of the designed test rig, which was introduced in [11]. A hub and a shaft coupling connected the specimen to the driving spindle. This configuration, rather than an outer-rotor setup, was chosen to protect the active parts of the spindle in case of a failure of the specimen at high speed. Each of the eight segments of the steel ring inside the FRP weighed 1.027 kg, and the distance between their center of gravity (CoG) and the rotation axis is about 55 mm. Hence, at 40,000 rpm one segment contained around 30 kJ of kinetic energy. The surrounding containment was designed to absorb this energy in case of specimen failure. The design criteria for the containment were derived from [12]. The containment also serves as a vacuum chamber. A detailed view of the spindle is shown in Figure 2b. The motor in the middle is a water cooled PMSM with four poles, a maximum torque of 9.6 Nm, and a maximum power of 30 kW. In order to avoid excessive wear of the high-speed drive, the rotor is supported by AMBs. The radial AMBs were designed in a heteropolar configuration with laminated cores on rotor and stator, both made out of 0.2 mm thick sheets of non-oriented silicon steel (NO20). The radial position of the rotor is measured with four eddy current sensors at each bearing, two for each radial direction.

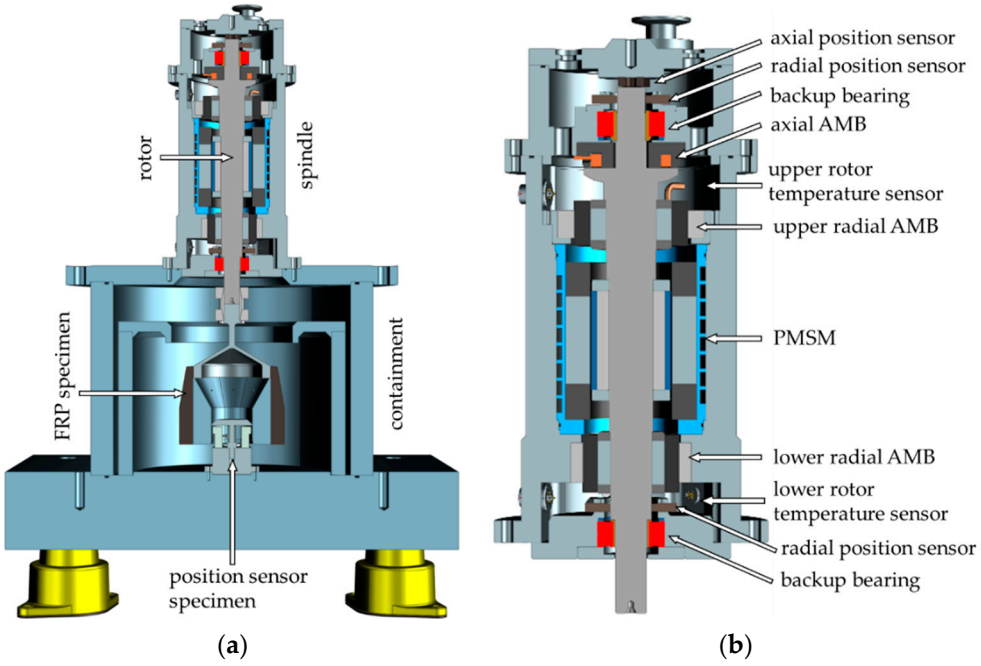

Figure 2. (**a**) Cross section of the test rig; (**b**) Cross section of the spindle.

To lift the combined mass of the spindle rotor and the specimen of roughly 20 kg, the axial AMB needs a large pole area, which leads to a big outer diameter of the thrust disk. Because of the high stress at high speed, a monolithic design was chosen (see [13]). The stator of the axial AMB was fabricated of the soft magnetic composite Siron S400b of the PMG Füssen GmbH [14]. An inductive sensor at the upper end of the rotor detects the axial position. Two-rowed hybrid spindle bearings with a static load rating of 20 kN are used as backup bearings. The rotor temperature is measured with two infrared sensors—one between the upper radial AMB and the thrust disk and one next to the lower radial position sensors, below the lower AMB. The moment of inertia of the specimen is about ten times higher than that of the rotor, and the surface speed of the specimen is more than two times higher. To protect the rotor and the spindle in case of a specimen failure, a predetermined breaking point was included in the hub (see Figure 3). This tapering also uncouples the dynamics of the rotor from the specimen to some extent.

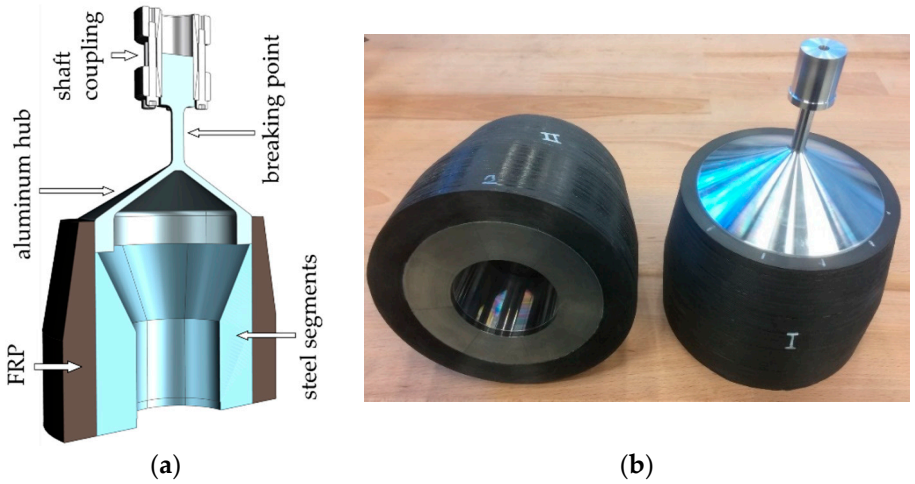

(**a**) (**b**)

Figure 3. (**a**) Cross section of the specimen; (**b**) Assembled specimens.

One goal of the test rig operation is to minimize the total test duration for one specimen, maximizing the number of specimens that can be tested in a given amount of time. The test rig should thus be operated with as much power as possible. High power normally leads to high losses, as well as subsequent heating. Losses on the stator can be effectively cooled with water, but without a medium for convection or thermal conduction through physical contact, the rotor can only transfer heat to the stator via radiation. Hence, even small power losses in the rotor can lead to a high rotor temperature. The temperature of the rotor is crucial for the feasibility of the cyclic fatigue testing, since the temperature of the specimen affects the strength of the FRP and can change the test result. Furthermore, the magnets of the PMSM should not be operated over a certain temperature. Thus, the overall goal of this paper is to minimize the test duration under the boundary condition of a maximum rotor and specimen temperature. For this purpose, the losses in the rotor during operation and their influence on the rotor temperature have to be identified. Furthermore, feasible methods of minimizing the most crucial losses in an existing test rig are derived.

2. Method

With the goal of finding the shortest total test duration, this paper proposes a structured approach to evaluate the heating of a magnetically levitated rotor in a vacuum, and deduces measures to avoid critical temperatures. An overview on the approach is shown in Figure 4. First, losses in the rotor of both radial AMBs, the axial AMB, and the PMSM were calculated for different rotational speeds, using transient electromagnetic 2D finite element (FE) models implemented in ANSYS Maxwell 2015. The highest and lowest operating speeds of the spindle followed from the demanded stress in the FRP, as described in Section 1.2. For each component, a polynomial was fitted to the related losses, to obtain

a mean loss value, which was used for the calculation of the steady state temperature. Next, air friction losses were calculated analytically, based on the kinetic theory of gases. Finally, to calculate the rotor temperature, a 3D-FE-model of a quarter of the test rig was set up and evaluated using ANSYS Workbench 19.1. Because of the water cooling, losses on the stator were not considered; instead the stator temperature in the simulation was predefined with measured data. A transient evaluation of the model was compared to measured temperatures on the test rig, to adjust thermal and loss calculation. To compute the rotor temperature after a long time of cycling, a steady state evaluation of the adjusted model was used. From this model, the most influential components on the rotor temperature can be derived. The focus was on components that allow for an improvement of the thermal behavior without major changes in the hardware. One option, which will be discussed as an example, is the reduction of the bias current in the radial AMBs [15]. Since this also changed the behavior of the rotor in the AMBs, a brief analysis of the rotor dynamics was performed using measurements and a mechanical 3D-FE-model of the rotor implemented in ANSYS Workbench 19.1. Another loss reduction can be achieved by reducing the control activity of the AMB [15]. Most of these strategies, like unbalance compensation (e.g., [16]) or a linear-quadratic-Gaussian-control (e.g., [17]), were not feasible at this point due to limitations of the AMB controller hardware. If no further loss reduction can be achieved in the components, the next step is to adjust the cycle time. Since rotational losses increase with speed and losses in the PMSM also increase with acceleration, the cycle time has a major influence on the mean losses and therefore on the rotor temperature. If the rotor temperature is below the critical values, the cycle time can be reduced. If the critical values are exceeded, the cycle time has to be increased. These options will be discussed further on.

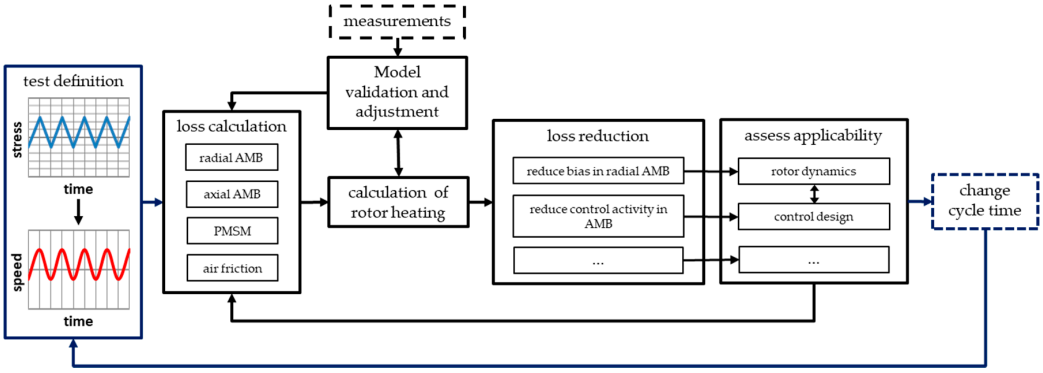

Figure 4. Applied approach to minimize the test duration by calculating and reducing rotor losses for the existing test rig.

3. Modeling of the Thermal Stability of the Rotor

The following sections discuss the loss calculation of the active magnetic bearings for the radial and axial direction and the electric machine, as well as losses caused by air friction. Subsequently, the thermal model focusing on the rotor temperature is described. For the model validation and potential adjustment, the calculation results are compared with measurements.

3.1. Loss Calculation of the Radial Active Magnetic Bearings

Both radial AMBs have eight poles, which are evenly distributed on the inner circumference of the stator and arranged in the sequence N–S–S–N–N–S–S–N. Flux leakage between two poles with equal flux direction—that is, N–N or S–S—is small, and thus two neighboring poles with differing flux direction, called a pole pair, function as one independent electromagnet. One pole pair of the upper radial AMB with an idealized average path of the magnetic flux φ is shown in Figure 5a. The magnetic flux of the AMB passes through the NO20-metal sheets that surrounded the solid rotor, which is shown in the bottom left corner. The nominal air gap between the rotor and the surrounding stator in the centered position is 0.4 mm. To linearize the actuator characteristic, a differential winding

design is used, where a common bias coil and a control coil, with associated currents, are used for two counteracting pole pairs [18]. In the test rig, two coils are mounted on each pole of the radial AMBs, the inner for bias current I_B and the outer for the control current I_Y. Both coils have the same number of turns. All bias coils are connected in series for one AMB and the control coils for each direction in one AMB. The magnetic flux in a specific point in the rotor changes direction each time it passed a pole with a different flux direction. The flux also drops between two poles with equal flux direction. This remagnetization leads to hysteresis losses P_h and excess losses P_e, as well as eddy currents and subsequent losses P_c. To calculate the losses, a transient electromagnetic 2D-FE-model of the rotor was set up and evaluated. Figure 5b shows the simulated magnetic flux density B distribution in a quarter of the upper radial AMB at a rotational speed of 30,000 rpm. Only the bias current of $I_B = 5.67$ A magnetized the rotor; the control current was set to zero. The flux density lay at 0.7 T on average, but locally exceeded the saturation flux density of the used NO20 sheets of 1.1 T.

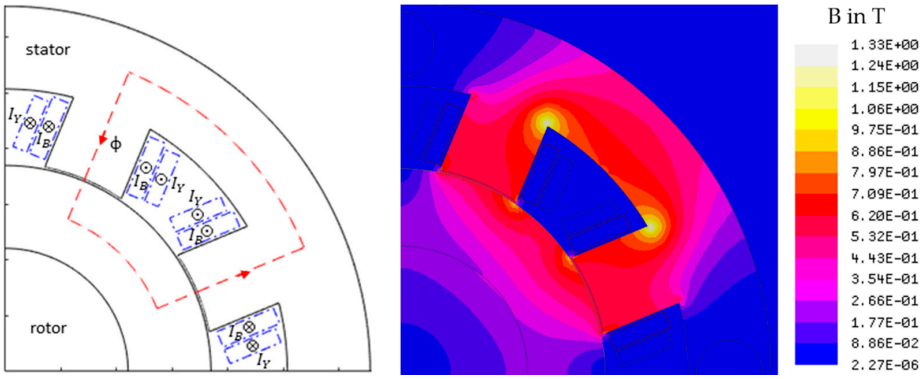

(**a**) (**b**)

Figure 5. (**a**) Quarter of the cross section of the upper radial active magnetic bearings (AMB); (**b**) Magnetic flux density in the upper radial AMB with only the bias current as excitation. The rotor turns clockwise.

For the loss calculation, the Bertotti formula [19] in the form of Equation (1) was applied, in which the three loss mechanisms P_c, P_h, and P_e depend on the amplitude of the flux density B_m and the frequency f with which the magnetic flux changes:

$$\begin{gathered} P_B = P_c + P_h + P_e, \text{ with} \\ P_c = \int k_c (f B_m)^2 \, dV, \;\; P_h = \int k_h f B_m^2 \, dV, \;\; \text{and} \;\; P_e = \int k_e (f B_m)^{1.5} \, dV. \end{gathered} \tag{1}$$

The corresponding loss constants k_c, k_h, and k_e were derived by fitting data from the manufacturer of the electric steel obtained by standardized measurements [20] to Equation (1), which yields:

$$k_{c,AMB} = 0.23 \, \frac{\mathrm{Ws}^2}{\mathrm{T}^2\mathrm{m}^3} \text{ and } k_{h,AMB} = 193.6 \, \frac{\mathrm{Ws}}{\mathrm{T}^2\mathrm{m}^3}.$$

For the NO20 sheets used in the radial AMBs, $k_{e,AMB}$ could not be significantly determined and therefore was set to zero. The calculated total iron losses for the upper and lower radial AMB are shown in Table 1. Additionally, the switching of the amplifiers leads to further high frequency changes in the magnetic flux. The resulting rotor losses can be calculated with the same model and yielded 0.11 W for the upper AMB and 0.09 W for the lower AMB.

Table 1. Rotational losses in the radial AMBs.

	15,000 rpm	**22,000 rpm**	**30,000 rpm**
Upper AMB	7.6 W	14.3 W	24.1 W
Lower AMB	6.3 W	11.8 W	19.8 W

3.2. Loss Calculation the of Axial Active Magnetic Bearing

The magnetic flux in the axial AMB is mostly symmetrical to the rotational axis, so no significant remagnetization losses should occur due to rotation. Nevertheless, the switching of the amplifier leads to changes in the magnetic flux and associated rotor losses. Equation (1) is only applicable for thin sheets, but in the solid thrust disk of the axial AMB, without the usage of a laminated core or soft-magnetic composites, eddy current losses dominate. Therefore, the other loss mechanisms were neglected. To calculate eddy current losses a transient electromagnetic 2D-FE-model was analyzed. Figure 6a shows the magnetic flux density B in the axial AMB, with an air gap of 0.4 mm and a coil current of 3.15 A. The resulting force is 200 N, which is required to lift the rotor with the specimen, with a total weight of 20.3 kg. Changes in the magnetic flux in the rotor result in eddy currents and therefore in a non-zero current density J in the rotor. Eddy current losses $P_{c,J}$ were calculated as the integral of the square of J over the rotor volume V, divided by the conductivity of the material σ_{el} (see Equation (2)). The conductivity of X14CrMoS17 is $\sigma_{el,rot} = 1.43 \times 10^6 \frac{1}{\Omega m}$.

$$P_{c,J} = \frac{1}{\sigma_{el}} \int J^2 dV. \tag{2}$$

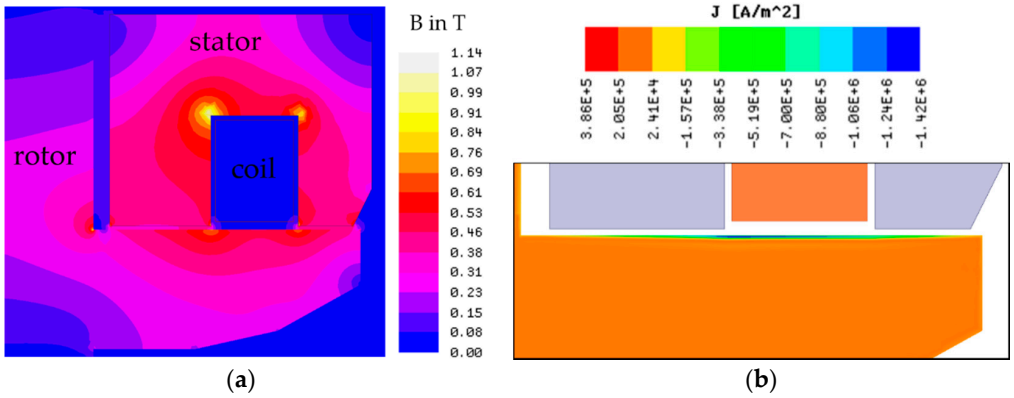

Figure 6. (**a**) Magnetic flux density in the axial active magnetic bearing (AMB); (**b**) Current density in the surface area of the thrust disk during switching of the axial AMB.

Since eddy currents oppose their provoking field, high frequency changes of the magnetic field only affect the outer layers of the conducting material. Hence, eddy currents are also limited to a thin region on the surface of the rotor (see Figure 6b). The losses of the axial AMB in the rotor due to the amplifier switching, derived by Equation (2), did not exceed 0.1 W.

3.3. Loss Calculation of the Permanent Magnet Synchronous Machine

The last active component that induces losses in the rotor is the PMSM. Here, the magnetic field rotates synchronously with the rotor. Remagnetization of the rotor occurs because of flux drops at slots in the stator and non-harmonic changes of the motor current due to switching of the inverter. Losses were calculated via a transient electromagnetic 2D-FE model. In the solid permanent magnets, losses were calculated using Equation (2), with an electric conductivity of the magnets of $\sigma_{el,mag} = 1.1 \times 10^6 \frac{1}{\Omega m}$. The rotor is laminated underneath the permanent magnets to further reduce losses. Remagnetization losses in these sheets were calculated according to Equation (1). The corresponding coefficients are:

$$k_{c,PMSM} = 0.12 \, \frac{\mathrm{Ws}^2}{\mathrm{T}^2\mathrm{m}^3}, \; k_{h,PMSM} = 166.7 \, \frac{\mathrm{Ws}}{\mathrm{T}^2\mathrm{m}^3}, \text{ and } k_{e,PMSM} = 3.24 \, \frac{\mathrm{Ws}^{1.5}}{\mathrm{T}^{1.5}\mathrm{m}^3}.$$

Results for different phase currents and rotational speeds are shown in Figure 7. The losses increased nearly linearly with the speed above 10,000 rpm. For root mean square values of the phase current (rms) below 10 A, losses were nearly independent of the phase current.

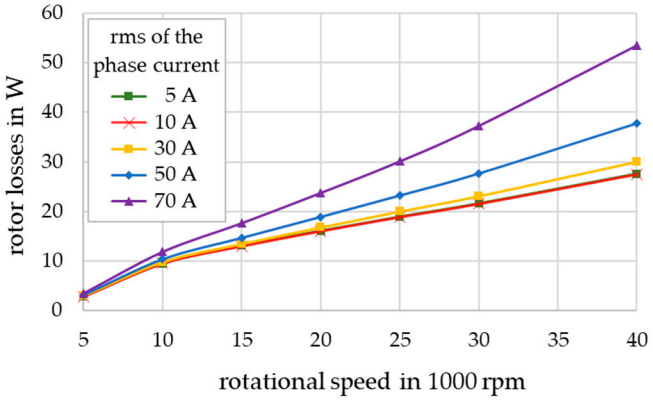

Figure 7. Rotor losses of the permanent magnet synchronous machine.

3.4. Air Friction Losses

For the calculation of air friction losses, it has to be evaluated if the gas in the system can be modeled with continuum dynamics. This was done by calculating the mean free path $\bar{l}$ of the gas. $\bar{l}$ is the avarage distance a molecule moves before it collides with another molecule of the gas. For a gas with pressure p, temperature T, and a mean atom diameter d_m, the mean free path $\bar{l}$ is calculated by Equation (3) (see [21]), where $k = 1.381 \times 10^{-23}$ $\frac{\mathrm{J}}{\mathrm{K}}$ is the Boltzmann constant,

$$\bar{l} = \frac{kT}{\sqrt{2}\pi p d_m^2}. \tag{3}$$

The mean molecule diameter of air is $d_m = 3.559 \times 10^{-10}$ m [21]. During rotation, the maximum pressure in the test rig is $p = 0.05$ Pa and the minimum temperature $T = 290$ K, resulting in a minimum mean free path of $\bar{l} = 0.144\ m$. Since $\bar{l}$ is much bigger than most of the air gaps in the test rig, an air molecule is more likely to collide with the walls of the test rig than with other air molecules. Hence, continuum dynamics are not applicable for this system. Instead, the kinetic theory of gases was utilized, where molecules are modeled as randomly moving elastic spheres. In [22], air friction losses P_a were derived by means of the momentum excange beween a spinning rotor and air molecules. For an axial disc with an outer radius r_o and an inner radius r_i this yields [22]:

$$P_{a,ax} = \pi p \sqrt{\frac{m_W \pi}{2kT}} \left(r_o^4 - r_i^4\right) \omega^2, \tag{4}$$

for a radial cylindrical surface with a radius r_r and a height h_r [22]:

$$P_{a,rad} = 4\pi p \sqrt{\frac{m_W \pi}{2kT}} h_r r_r^3 \omega^2, \tag{5}$$

and for a truncated cone with a height h_c, a lower radius r_l and an upper radius r_u:

$$P_{a,rad} = \pi p \sqrt{\frac{m_W \pi}{2kT}} \frac{\sqrt{(r_l - r_u)^2 + h_c^2}}{r_l - r_u} \left(r_l^4 - r_u^4\right) \omega^2, \tag{6}$$

where ω is the rotational speed of the rotor and m_W is the mean molecule mass of the gas. Hence, air friction losses increase linearly with p, quadratically with ω, and decrease with T. For dry air,

the mean atom mass is approximately $m_W \approx 4.81 \times 10^{-26}$ kg [21]. The losses were calculated for each surface of the rotor and the specimen and were subsequently superimposed. For the worst case, with a maximum pressure of $p = 0.05$ Pa and a minimum temperature of $T = 290$ K, the sums of the calculated losses for the rotor and the specimen at different speeds are listed in Table 2.

Table 2. Air friction losses in the test rig with $p = 0.05$ Pa and $T = 290$ K.

	15,000 rpm	30,000 rpm
rotor	0.016 W	0.066 W
specimen	0.283 W	1.131 W

3.5. Simulation of Thermal Rotor Behavior

The thermal simulation was performed using a 3D-FE model of a quarter of the test rig, both with and without the specimen. The rotor transmits thermal energy to the stator via radiation, and vice versa. It was assumed that the emissivity and absorptivity of the rotor and stator surfaces do not depend on the wavelength or direction of the radiation. Under this assumption, the emissivity and absorptivity of the surface are equal [23]. For real materials, only a part of the radiation that hits a surface is absorbed while the rest is reflected, hence, the coefficient of emission is smaller than one. When considering the heat exchange between two surfaces through radiation, both surfaces have to be taken into account. Consequently, for the simulation of the rotor heating, the inner surface of the stator has to be included in the model. The stator and rotor were painted with lacquer on the surface of the AMBs and the PMSM. The coefficient of emission was assumed to be 0.9 for all painted parts and the FRP. For the unpainted, blank parts of the steel rotor, a coefficient of emission of 0.3 was assumed, and for the aluminum parts of the stator and the specimen a value of 0.05 was assumed [23]. The temporal stator temperature profile of the active components was roughly approximated with three measured temperatures, which were linearly interpolated. The temperature values can be found in Appendix A. This transient temperature change has only a small impact on the simulation results; using a constant mean temperature value for all stator components increases the calculated rotor temperature only about 1 °C. For the rest of the stator, a constant temperature of 25 °C was predefined. To obtain the temperature distribution in the rotor, heat conduction in the rotor was also taken into account in the model, with a conductivity of 25 W/Km. Calculating the steady state rotor temperature during the test cycles requires the mean loss value per cycle for each actuator. As a baseline, a cycling time of 30 s was defined—i.e., during one cycle, the rotor constantly accelerates for 15 s from 15,000 rpm to 30,000 rpm, and then constantly decelerates with the same slope back to 15,000 rpm. The rotational speed and the speed dependent losses of the active components are illustrated in Figure 8a. The mean values of all calculated losses are shown in Figure 8b.

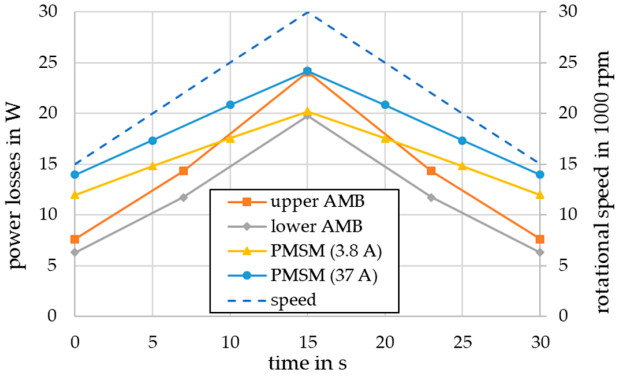

(**a**)

Mean losses	
Upper AMB	15.3 W
PMSM (3.8 A)	16.2 W
PMSM (37 A)	19.1 W
Lower AMB	12.6 W
Axial AMB	0.1 W
Air friction	0.7 W

(**b**)

Figure 8. (**a**) Rotational speed and calculated rotational losses of the active components during one cycle; (**b**) Resulting mean losses of all calculated loss mechanisms in the rotor during cycling.

3.6. Temperature Measurements

To validate the described models, the rotor temperature was measured during cycling without a specimen. Two infrared sensors measured the rotor temperature: one between the upper radial AMB and the thrust disk and one next to the lower radial position sensors (see Figure 2b). The utilized sensors can measure the temperature of metallic surfaces above 50 °C, with an uncertainty of ±2 °C. First, the cooling of the levitated but not spinning rotor from a known temperature was analyzed. This excluded the rotational losses and the switching losses in the PMSM. Hence, only the small switching losses of the AMBs were present. The results of a transient simulation and the measurement are shown in Figure 9a. With a maximum deviation of 1.85 °C, the simulation results lie in the range of the measurement uncertainty. Consequently, the switching losses of the AMBs and the modeling of the heat transfer are sufficiently accurate. Next, the thermal behavior of the rotor during rotation was analyzed. Before the measurement, the system was turned off for 12 h, to ensure the rotor was cooled down to room temperature. During the measurement, the PMSM continuously accelerated and decelerated the rotor without a specimen from 15,000 rpm to 30,000 rpm. In the transient simulation, the mean losses from Figure 8b were used. The initial speed up to 15,000 rpm, which takes about 15 s, was neglected. Figure 9b compares the measured temperatures at both sensor positions with the simulation. While the rotor temperature at both positions was nearly the same in the simulation, it differed considerably in the measurement. The model underestimated the rotor heating at both measurement positions. At the lower position, the deviation was 5.2 °C, while it was 22.4 °C at the upper position. Due to the good agreement of the rotor cooling, the modeling error is expected to lie in the loss calculation rather than the thermal model.

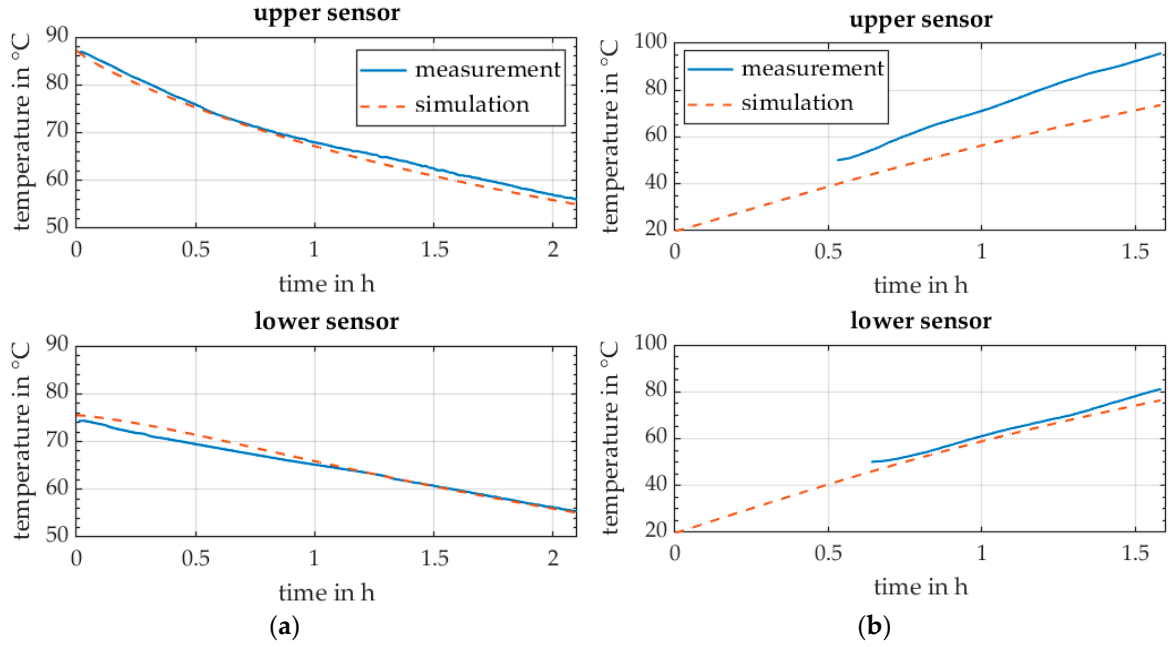

Figure 9. (**a**) Simulated and measured rotor cooling without the specimen; (**b**) Simulated and measured rotor temperatures without the specimen during cycling.

One reason why the losses could be underestimated can be found in the loss coefficients of the NO20 sheets in the AMBs and PMSM. The loss measurements done by the manufacturer that were used to identify the loss coefficients are normally performed on unmachined sheets after a precise annealing process. However, the material behavior can change during milling and heating. For example, a damaged sheet isolation can increase eddy current losses by up to 30% [24] and hysteresis losses can vary more than 50% depending on their heat treatment [25]. Because these changes can hardly be quantified, the calculated losses are adjusted to fit the temperature measurement. At the lower AMB,

the calculated losses were increased by 10% to fit the temperature at the lower temperature sensor. Since the sheets at the upper and lower AMB were milled and heated similarly, the losses in the upper AMB increased by 10% as well. To further match the simulation with the measured temperature at the upper sensor, 8 W of additional losses in the axial AMB were required in the simulation. For the loss calculation, it was assumed that the axial AMB is perfectly symmetrical with respect to the rotational axis. In reality, small circumferential variations in the material of stator and rotor lead to flux changes during rotation and hence to higher rotor losses. Furthermore, control activities in the AMBs were neglected in the simulation, but during the measurement, considerable movement in the axial direction was observed. The adjusted losses are summarized in Table 3. A transient thermal simulation with the adjusted loss values showed good accordance with the measured data (see Figure 10a).

Table 3. Adjusted mean losses in the rotor during cycling.

Axial AMB	Upper AMB	Lower AMB
8.1 W	16.9 W	13.8 W

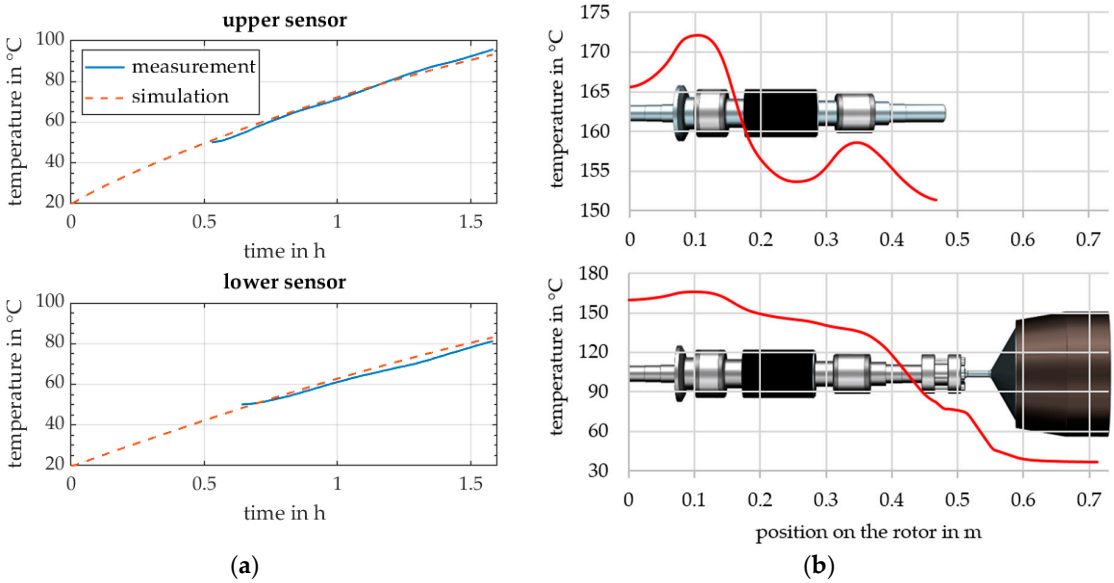

Figure 10. (**a**) Simulated and measured rotor temperatures with adjusted AMB losses without the specimen during cycling; (**b**) Simulated steady state temperature of the rotor with and without the specimen.

With the adjusted loss values, a steady state thermal simulation of the test rig with and without the specimen was performed. Without the specimen, the motor needs an rms phase current of 3.8 A to accelerate the rotor during the described cycle, but with the specimen an rms phase current of about 37 A is required. The losses of the PMSM were considered accordingly in the simulation. The other losses in the rotor were assumed to be equal for both cases. The simulated temperature distribution in the center of the rotor over the axial length is shown in Figure 10b. In the specimen, the temperature between the FRP and the steel segments is displayed. The maximum temperature without a specimen was 176 °C, located at the upper AMB. Even though higher rotor losses occur with the specimen, the rotor temperature was 10 °C lower than without it, as the large surface area of the FRP benefits heat transfer to the surrounding containment. The thin tapering at the hub led to a large temperature drop between rotor and specimen, preventing the temperature of the FRP from exceeding 40 °C. The operation temperature of the FRP in the flywheel must not exceed 80 °C. The magnets of the PMSM should not be operated over 120 °C. In order to have a safety margin, the magnet temperature should not exceed 110 °C. The simulation results, however, show a temperature of the magnets of over 140 °C. Thus, to avoid reducing the cycle time, rotor losses have to be reduced.

4. Loss Reduction

As seen in the previous section, the highest power losses in the rotor were due to rotational losses in the radial AMBs and PMSM, as well as switching losses in the PMSM, which all a have similar order of magnitude. Losses due to control activities in the axial AMB were slightly lower. Switching in the AMBs and air friction can be neglected. Hence, the main focus should be on the reduction of rotational losses in the radial AMBs and the PMSM as well as switching losses in the PMSM. In this paper only the radial AMBs will be further discussed.

4.1. Reducing Losses in the Radial Bearings

One effective way to reduce the rotational losses of an AMB is to reduce its bias current I_B. For example, reducing I_B from 5.67 A to 4 A reduces the rotational losses in the rotor by more than 50%, to 8.2 W in the upper AMB and 6.8 W in the lower AMB. A thermal simulation and measurement with $I_B = 4$ A was performed, where the rotor was again cycled according to Figure 8a. The results are shown in Figure 11. The transient simulation and the measurement of the test rig without a specimen again show sufficient correspondence (see Figure 11a). The steady state simulation predicted a maximum temperature of 129 °C at the axial AMB and 123 °C at the PMSM without a specimen, as well as 127 °C and 117 °C with a specimen (see Figure 11b). Changing I_B also changes the rotor dynamics in the AMBs. To evaluate the possibility of a bias reduction, the dynamics of the levitated rotor will be investigated in the next section.

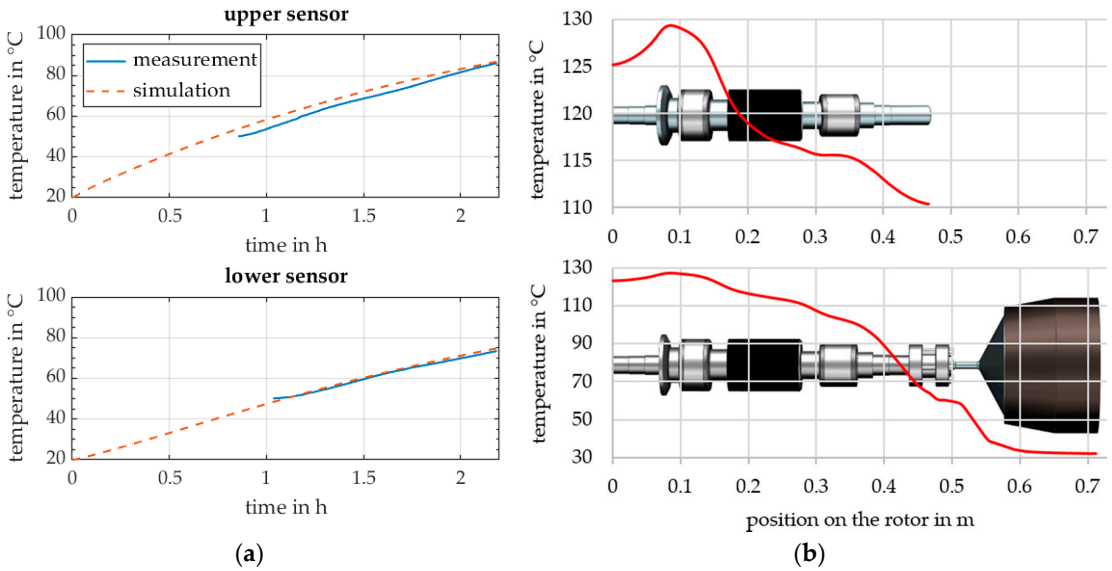

Figure 11. (**a**) Simulated and measured rotor temperatures with a reduced bias current of 4 A in both AMBs without the specimen during cycling; (**b**) Steady state rotor temperature with a reduced bias current of 4 A in both AMBs with and without the specimen.

4.2. Rotor Dynamics

A mechanical 3D-FE model of the rotor was created and evaluated. For a modal analysis of the model, the AMBs were modeled as springs with a constant stiffness of 2.5×10^5 N/m. The first bending mode of the rotor without a specimen lay at 1,030 Hz, thus 353 Hz above the highest rotational frequency. The calculated second bending mode was at 2,170 Hz. Measured Campbell diagrams of the rotor without the specimen are shown in Figure 12. They were derived from the signals of the radial position sensors of the AMBs during an acceleration of the rotor from 0 rpm to 40,000 rpm in 110 s. The signals were filtered with a 5 kHz low-pass filter and sampled with 10 kHz. To create the Campbell diagram, the measurement was divided into 4096 sample long windows, and for each window a Fourier transformation was performed. Figure 12a shows the Campbell diagram of the position data

of the upper AMB with $I_B = 5.67$ A. The lines starting at the lower left corner are harmonics of the rotational speed, the thickest one being the first harmonic. Odd harmonics of the rotational speed are clearly visible, whereas even harmonics are barely detectable. The approximately horizontal lines are eigenfrequencies (EFs) of the system. At about 90 Hz lies the rigid body tilting mode of the rotor in the AMBs. The translational rigid body mode is not visible in the diagram. The first bending mode of the rotor can be seen at 1057 Hz, the second at 2063 Hz. The second splits into a forward and backward mode. While the calculated first bending mode only differed by 27 Hz, the second bending mode was about 100 Hz lower than the simulation predicted. Underneath each Campbell diagram, the mean deflection of the rotor for each window is shown. The deflections were less than 20% of the backup bearing clearance of 200 µm. Peaks can be seen when the rotational speed or its harmonics hit an EF. The first two peaks were due to the rigid body modes. The next peak at 25,000 rpm was caused by the fifth harmonic reaching the forward mode of the second bending EF, and the last peak at 39,000 rpm was caused by the third harmonic reaching the backward mode of the second bending EF. Smaller peaks can also be seen when higher harmonics reach the second bending EF, where every second odd harmonic excited its forward mode and every other odd harmonic excited the backward mode. A notch filter was placed at 1 kHz in the AMB control, so there was no additional excitation of this EF due to harmonics of the rotational speed. Figure 12b shows the same evaluations for $I_B = 4$ A. The harmonics were not influenced by I_B and the EFs only changed slightly. However, the amplitude of the deflection differed noticeable. The peak where the first harmonic crossed the second rigid body mode was about 30% higher with a reduced I_B, whereas the peaks at higher speeds were now below 20 µm. Because the normal speed range starts at 15,000 rpm, the rigid body mode has to be crossed only once per test, while the peak at 25,000 rpm is reached twice every cycle. Consequently, without a specimen, reducing I_B does not only reduce the rotational losses, but also reduces the control activity of the AMB during cycling.

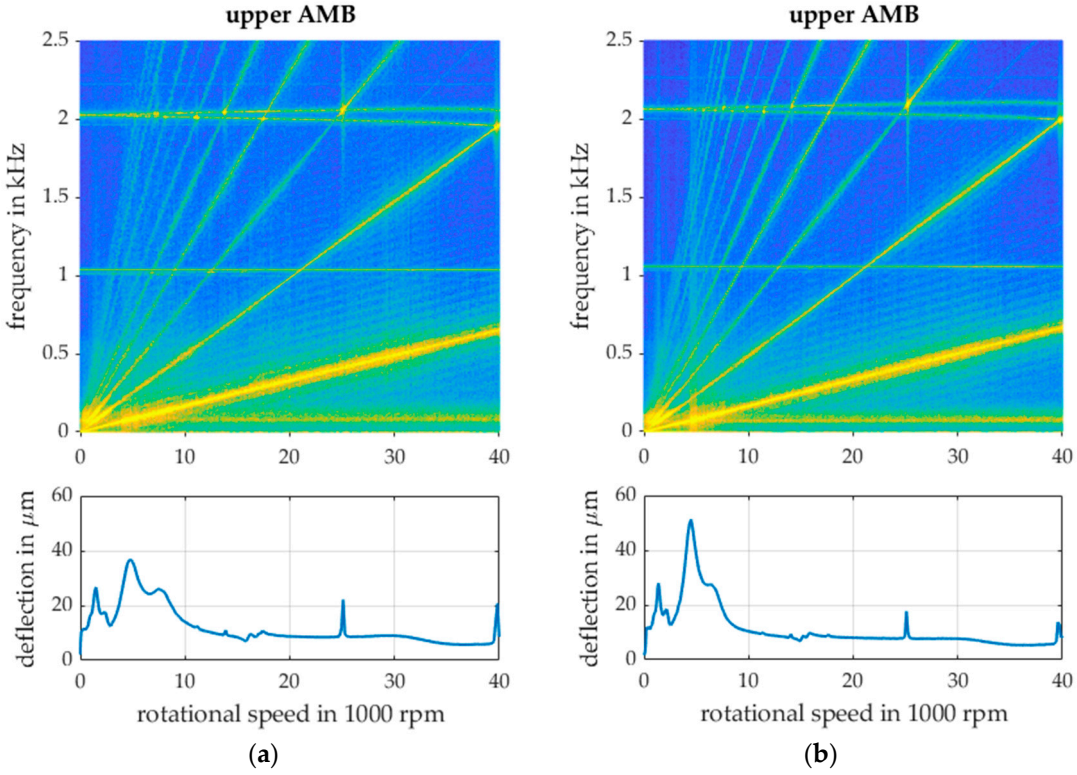

Figure 12. (**a**) Measured Campbell diagram and deflection of the rotor with a bias current of 5.67 A without specimen; (**b**) Measured Campbell diagram and deflection of the rotor with a reduced bias current of 4 A without specimen.

Measurements with a specimen were not performed yet, but Figure 13a shows the calculated EFs and Figure 13b the simulated Campbell diagram of the rotor with the specimen. The first elastic mode was at 9 Hz, where only the specimen tilts at the tapering. At speeds higher than 9 Hz, the CoG of the specimen did not move translationally. In the second, third, and fourth modes, the specimen was tilting around its CoG and in the fifth mode it does not move at all. The rotor showed elastic deformations beginning with the fourth mode. Due to the high inertia ratio of the specimen, the higher EFs showed a strong dependency on the rotational speed, which can be seen in the Campbell diagram in Figure 13b. The first three EFs were below 250 Hz, where the fatigue testing begins, and have to be passed while starting a test. The fourth EF increased in such a way that it is not reached by speed-synchronous excitations within the operation range. However, due to the close proximity of the fourth mode, the bandwidth of the AMBs has to include this frequency. The fifth EF had a minimum distance of 290 Hz to the rotational speed and therefore it will have to be filtered out from the position signal.

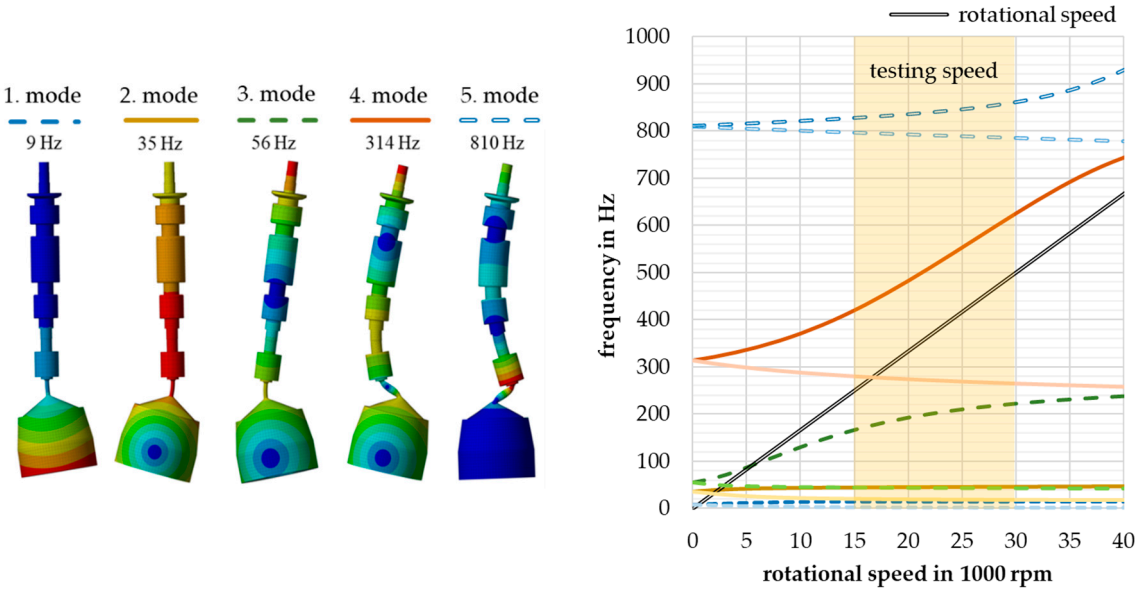

Figure 13. (**a**) Calculated bending eigenmodes below 1 kHz of the rotor with sample; (**b**) Calculated Campbell diagram of the rotor with the specimen. Each eigenmode shown in (**a**) splits in a forward and a backward mode.

For the differential winding design, which is used for the radial AMBs, the control current has to be smaller than I_B. To allow control currents bigger than I_B the AMBs would have to be rebuilt for a differential control design and a nonlinear control might be needed (see [15,26–28]). Both would require major changes in the hardware. Hence, with the existing hardware, reducing I_B also reduces the maximum force the actuators can generate. In the centered position, one AMB can generate a force of 278 N with $I_B = 5.67$ A, but only 144 N with $I_B = 4$ A. For the rotor without a specimen this is unproblematic, because there are nearly no external loads in the test rig and the rotor can be precisely balanced to minimize unbalance forces. However, the initial unbalance of an assembled specimen is big and balancing it precisely is difficult. The force generated by the AMB has to be big enough to counteract the unbalance force while passing the first three EFs. This has to be further investigated.

4.3. Increasing the Cycle Time

When no further loss reduction can be achieved, the cycle time has to be changed. In the upper example, even with a bias current of 4 A, the rotor temperature were above 110 °C but below 120 °C, as shown in Section 4.1. If further bias reduction or other loss reduction strategies are not applicable, a less favorable possibility to reduce the rotor temperature is to increase the cycle time. Here, two variations

were considered, which are illustrated in Figure 14a. In the first variation, the acceleration of the rotor is reduced to lower load dependent losses in the PMSM, in the second variation, after a cycle, the rotational speed is held constant at 15,000 rpm for a while to allow the rotor to cool down. How long the cycle has to be increased depends on the associated loss reduction and the maximum allowable rotor temperature. For example, the cycle time could be increased from 30 s to 37 s to reduce the rms motor phase current from 37 A to 30 A, and thereby the rotor losses in the PMSM by 1.7 W to 17.4 W. Losses in the AMBs stay the same. Alternatively, after a 30 s cycle, the speed is held constant at 15,000 rpm for 7 s. Here, the mean losses can be calculated by averaging the mean losses for the first 30 s, as shown in Sections 3.5 and 3.6, and the losses at a constant speed. To keep the rotor without a specimen at a constant speed of 15,000 rpm, an rms phase current of 1.8 A is needed in the PMSM. Hence, it was assumed that an rms phase current of less than 10 A is needed to keep the rotor with a specimen at constant speed. Below 10 A, losses were nearly independent of the phase current (see Section 3.3). The resulting mean losses are summarized in Table 4. For the axial AMB constant, rotor losses of 8.1 W were assumed for both variations. The total cycle time in both variations was 37 s and the whole test would take the same amount of time—86 days to perform 200,000 cycles.

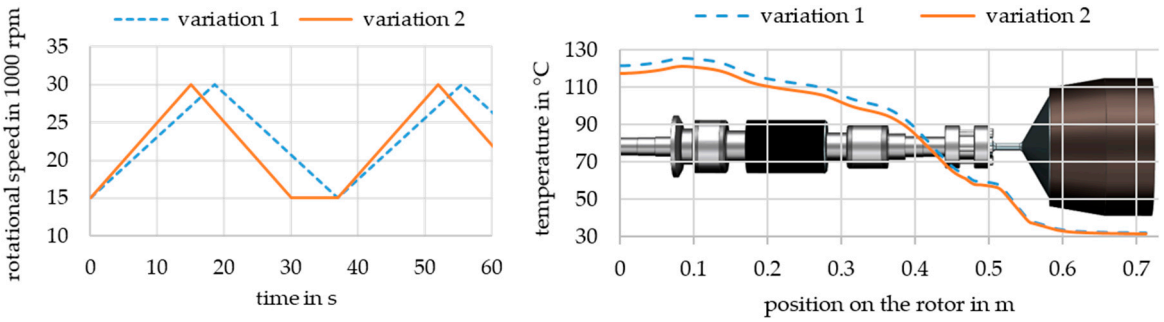

Figure 14. (**a**) Variations of increasing the cycle time to reduce the rotor temperature; (**b**) Steady state rotor temperature of both cycle variations with a reduced bias current of 4 A in both AMBs with a specimen.

Table 4. Mean rotor losses during cycling variation 1 and 2 with a reduced bias current of 4 A.

	Upper AMB	PMSM (30 A)	PMSM (37 A)	Lower AMB	Air Friction
Variation 1	8.2 W	17.4 W	-	6.8 W	0.70 W
Variation 2	7.5 W	-	17.7 W	6.2 W	0.59 W

Since losses in the PMSM showed only a small dependency on the load, the total mean losses in variation 2 were smaller than in variation 1. The calculated rotor temperature is shown in Figure 14b. For variation 1, the maximum calculated temperature in the permanent magnets of the PMSM was 115.6 °C, and for variation 2 it was 111.0 °C. Thus, with a slightly increased cooling time at 15.000 rpm, variation 2 should not reach the critical magnet temperature, whereas variation 1 has no big benefit for the rotor temperature. However, in the model the thermal conduction between rotor and magnets of the PMSM is assumed as ideal. In reality, small gaps could decrease the conductivity and therefore increase the dependency of the magnet temperature on the internal losses of the PMSM. This would make the loss reduction in the PMSM critical compared to the other components, giving variation 1 higher relevance.

5. Discussion

This paper proposed a structured approach to evaluate the heating of a magnetically levitated rotor in a vacuum, and deduced measures to avoid critical temperatures. First losses and the subsequent rotor heating were calculated. The rotational losses in the radial AMBs and the PMSM were identified as the

main rotor loss mechanisms in the test rig. Losses in the axial AMB during rotation are smaller but also in the same order of magnitude. Switching losses in the AMBs and air friction losses only have a very small contribution to the total losses. One way to achieve loss reduction in the radial AMBs, without major changes in the spindle hardware, is to reduce the bias current. While doing so, the controllability of the rotor has to be ensured. The applicability of this approach was shown for the rotor without a specimen, but was not yet shown with a specimen. Stability problems could arise at low rotational speeds where many EFs can be excited. An adjustment of the bias with the rotational speed might be necessary. Further loss reduction can be accomplished by reducing the control activity. A centralized control of the radial AMBs should reduce the activities in the upper radial AMB. To realize a centralized control, however, the amplifier needs to be replaced. An overview of loss reduction strategies in AMBs can be found, for example, in [15]. Losses in the PMSM can be reduced by increasing the switching frequency of its inverter or by employing an output filter. Both options also require changes in the hardware. If no further loss reduction can be achieved, the cycle time has to be adjusted, so that the critical rotor temperature is exactly reached. In the present case, the cycle time had to be increased. With a cycle time of 37 s and a bias current of 4 A in both radial AMBs, a calculated steady state temperature of 111 °C can be reached, however, this has the drawback of an increased test duration. To account for modeling errors, the cycle time can further be adjusted during operation, depending on the rotor temperature, in a closed control loop. For the calculations, a constant thermal conductivity in the rotor was assumed. This assumption is especially critical between the magnets and the rotor. In reality, the thermal coupling will be poorer, resulting in a higher magnet temperature.

Author Contributions: Conceptualization, D.F., M.S. and M.R.; methodology, D.F., M.S.; validation, D.F.; formal analysis, D.F.; investigation, D.F.; resources, D.F.; data curation, D.F.; writing—original draft preparation, D.F.; writing—review and editing, D.F., M.S., M.R. and S.R.; visualization, D.F..; supervision, S.R.; project administration, D.F. and S.R.

Funding: This research was funded by the German Federal Ministry for Economic Affairs and Energy, grant number 03ET6064A.

Conflicts of Interest: The authors declare no conflict of interest. The funders had no role in the design of the study; in the collection, analyses, or interpretation of data; in the writing of the manuscript, or in the decision to publish the results.

Appendix A

The following Table A1 shows the measured stator temperature of the test rig during cool down. Table A2 shows the same temperatures during cycling with a bias current of 5.67 A and Table A3 shows them during cycling with a bias current of 4 A. These temperatures were used in their corresponding simulations.

Table A1. Measured stator temperature during cool down.

Time in s	axial AMB	Time in s	Upper AMB	Lower AMB	Time in s	Motor
0	25.0 °C	0	38.8 °C	40.9 °C	0	35.4 °C
4500	23.1 °C	2500	35.7 °C	37.3 °C	550	23.3 °C
7600	22.5 °C	7600	34.6 °C	35.6 °C	7600	22.3 °C

Table A2. Measured stator temperature during cycling with a bias current of 5.67 A.

Time in s	Axial AMB	Time in s	Upper AMB	Lower AMB	Time in s	Motor
0	18.6 °C	0	18.9 °C	18.9 °C	0	20.7 °C
1800	22.4 °C	1600	43.0 °C	45.3 °C	800	35.2 °C
5720	25.9 °C	5720	51.1 °C	53.3 °C	5720	35.5 °C

Table A3. Measured stator temperature during cycling with a bias current of 4 A.

Time in s	Axial AMB	Time in s	Upper AMB	Lower AMB	Time in s	Motor
0	18.5 °C	0	18.9 °C	19.0 °C	0	20.2 °C
2800	23.0 °C	1850	32.7 °C	34.9 °C	800	35.2 °C
8000	25.0 °C	8000	38.8 °C	40.9 °C	8000	35.4 °C

References

1. Sebastián, R.; Peña-Alzola, R. Flywheel energy storage systems: Review and simulation for an isolated wind power system. *Renew. Sustain. Energy Rev.* **2012**, *16*, 6803–6813. [CrossRef]
2. Amiryar, M.E.; Pullen, K.R. A Review of flywheel energy storage system technologies and their applications. *Appl. Sci.* **2017**, *7*, 286. [CrossRef]
3. Mason, P.; Howe, D.; Atallah, K. Soft Magnetic Composites in Active Magnetic Bearings. In Proceedings of the IEE Colloquium on New Magnetic Materials—Bonded Iron, Lamination Steels, Sintered Iron and Permanent Magnets, London, UK, 28 May 1998. [CrossRef]
4. Pichot, M.A.; Driga, M.D. Loss reduction strategies in design of magnetic bearing actuators for vehicle applications. *IEEE Trans. Magn.* **2005**, *41*, 492–496. [CrossRef]
5. Schaede, H.; Richter, M.; Quurck, L.; Rinderknecht, S. Losses in an Outer-Rotor-Type Kinetic Energy Storage System in Active Magnetic Bearings. In Proceedings of the 14th International Symposium on Magnetic Bearings, Linz, Austria, 11–14 August 2014.
6. Quurck, L.; Richter, M.; Schneider, M.; Franz, D.; Rinderknecht, S. Design and practical realization of an innovative flywheel concept for industrial applications. In Proceedings of the SIRM 2017–12 Internationale Tagung Schwingungen in Rotierenden Maschinen, Graz, Austria, 15–17 February 2017; pp. 151–160. [CrossRef]
7. Arnold, S.M.; Saleeb, A.F.; Al-Zoubi, N.R. Deformation and life analysis of composite flywheel disk systems. *Compos. Part B Eng.* **2002**, *33*, 433–459. [CrossRef]
8. ISO 527-5, Plastics—Determination of Tensile properties—Part 5: Test Conditions for Unidirectional Fibre-Reinforced Plastic Composites. Available online: http://www.iso.org/standard/52991.html (accessed on 2 May 2019).
9. ISO 14126, Fibre-Reinforced Plastic Composites—Determination of Compressive Properties in the in-Plane Direction. Available online: https://www.iso.org/standard/23638.html (accessed on 2 May 2019).
10. Knops, M. *Analysis of Failure in Fiber Polymer Laminates*; Springer: Berlin/Heidelberg, Germany, 2008; Volume 2. [CrossRef]
11. Franz, D.; Schneider, M.; Richter, M.; Rinderknecht, S. Magnetically levitated spindle for long term testing of fiber reinforced plastic. In Proceedings of the 16th International Symposium on Magnetic Bearings, Beijing, China, 13–17 August 2018.
12. Hagg, A.C.; Sankey, G.O. The containment of disk burst fragments by cylindrical shells. *ASME J. Eng. Power* **1974**, *96*, 114–123. [CrossRef]
13. Larsonneur, R. Design and Control of Active Magnetic Bearing Systems for High Speed Rotation. Doctoral dissertation, Swiss Federal Institute of Technology Zuerich, Zuerich, Switzerland, 1990. [CrossRef]
14. Schoppa, A.; Delarbre, P. Soft magnetic powder composites and potential applications in modern electric machines and devices. *IEEE Trans. Magn.* **2014**, *50*. [CrossRef]
15. Gaechter, S.; Kameno, H.J. Application of zero-bias current active magnetic bearings to flywheel energy storage systems. *Koyo Eng. J.* **2004**, *165*, 25–30.
16. Herzog, R.; Bühler, P.; Gähler, C.; Larsonneur, R. Unbalance compensation using generalized notch filters in the multivariable feedback of magnetic bearings. *IEEE Trans. Control Syst. Technol.* **1996**, *4*, 580–586. [CrossRef]
17. Barbaraci, G.; Pesch, A.H.; Sawicki, J.T. Experimental investigations of minimum power consumption optimal control for variable speed AMB rotor. In Proceedings of the ASME 2010 International Mechanical Engineering Congress & Exposition, Vancouver, BC, Canada, 12–18 November 2010. [CrossRef]
18. Schweitzer, G.; Maslen, E.H. *Magnetic Bearings*; Springer: Berlin/Heidelberg, Germany, 2009. [CrossRef]

19. Bertotti, G. General properties of power losses in soft ferromagnetic materials. *IEEE Trans. Magn.* **1988**, *24*, 621–630. [CrossRef]
20. IEC 60404-2, Magnetic Materials—Part 2: Methods of Measurement of the Magnetic Properties of Electrical Steel Strip and Sheet by Means of an Epstein Frame. Available online: https://webstore.iec.ch/publication/62746 (accessed on 2 May 2019).
21. Jousten, K. *Handbook of Vacuum Technology*, 2nd ed.; Wiley-VCH Verlag: Weinheim, Germany, 2012. [CrossRef]
22. Koch, R. Schwung-Energiespeicher-System mit Supraleitendem Magnetlager. Ph.D Thesis, University of Stuttgart, Stuttgart, Germany, 2002.
23. Baehr, D.B.; Stephan, K. *Heat and Mass Transfer*, 3rd ed.; Springer: Berlin/Heidelberg, Germany, 2011. [CrossRef]
24. Müller, G.; Vogt, K.; Ponick, B. *Berechnung elektrischer Maschinen*, 6th ed.; Wiley-VCH Verlag: Weinheim, Germany, 2009. [CrossRef]
25. Canders, W.R. Berechnung von Eisenverlusten—Physikalisch Basierter Ansatz Nach Bertottis Theorie. Annual report, Braunschweig, Germany. 2011. Available online: https://www.tu-braunschweig.de/Medien-DB/imab/09-Jahresberichte/2010-11/07_Canders_2010_11.pdf (accessed on 2 May 2019).
26. Lévine, J.; Lottin, J.; Ponsart, J.C. A nonlinear approach to the control of magnetic bearings. *IEEE Trans. Control Syst. Technol.* **1996**, *4*. [CrossRef]
27. Wilson, B.C.; Panagiotis, T.; Heck-Ferri, B. Experimental validation of control designs for low-loss active magnetic bearings. In Proceedings of the AIAA Guidance, Navigation and Control Conference 2005, San Francisco, CA, USA, 15–18 August 2005. [CrossRef]
28. Grochmal, T.R.; Lynch, A.F. Nonlinear control of an active magnetic bearing with bias currents: experimental study. In Proceedings of the 2006 American Control Conference, Minneapolis, MN, USA, 14–16 June 2006. [CrossRef]